Precision Engineering 34 (2010) 345–356

Contents lists available at ScienceDirect

Precision Engineering

journal homepage: www.elsevier.com/locate/precision

Torsional and axial frequency response prediction by RCSA

Tony L. Schmitz*

University of Florida, Department of Mechanical and Aerospace Engineering, PO Box 116300, Gainesville, FL 32611-6300, United States

ARTICLE INFO

Article history:
Received 11 March 2009
Received in revised form 5 August 2009
Accepted 20 August 2009
Available online 29 August 2009

Keywords:
Milling
Drilling
Dynamics
Coupling
Substructure
Receptance

ABSTRACT

This paper describes the application of Receptance Coupling Substructure Analysis (RCSA) to the prediction of torsional and axial, as well as bending, receptances. The coupling equations are developed and used to compare predictions to experimental results for a stepped diameter free–free beam and two tool-holder-spindle assemblies.

1. Introduction

Many research studies over the past several decades have identified the relationship between the dynamics of the cutting tool-support structure-workpiece and the machining process, including turning, milling, boring, and drilling. Comprehensive reviews of these studies are provided in [1–8], for example. Due to the cutting force, time-dependent deflections between the tool and workpiece are obtained. The relationship between the steady-state deflection and applied force is described by the system frequency response function (FRF), or receptance. Depending on the force direction and structure geometry, the relevant receptances may describe (lateral) bending, torsion, and/or axial vibration behavior.

While experimental techniques, such as impact testing, may often be applied to determine the required receptances directly, in some instances this approach may prove too time-consuming (such as a large production facility with many hundreds of tooling combinations) or inconvenient due to physical restrictions (slender, flexible tools and micromills). In these situations, a preferred alternative is to implement a predictive technique based on tool-structure models. Challenges to this paradigm include damping estimation, particularly at interfaces, contact stiffness determination, in rolling element bearings, for example, and full geometric knowledge of commercial components, such as spindles. To address these obstacles, the Receptance Coupling Substructure Analysis (RCSA) procedure was developed [9–13] by building on the receptance coupling principles detailed by Bishop and Johnson [14]. Using RCSA, models of the tool and holder (amenable to modeling) are coupled to a measurement of the spindle-machine (more difficult to model) to predict the assembly's bending receptances. This information may then be used, together with milling models, to predict the stability [15,16] and forced vibration behavior [17].

In this paper, the RCSA method is extended to prediction of torsional and axial receptances, in addition to bending responses, for tool-holder-spindle assemblies. The goal of the paper is to provide readers with a straightforward approach to coupling models of tools and holders with spindle-machine dynamics. While the scope of this study is limited to the coupling procedure, it is also shown experimentally that tool model development is an important related topic. Although analytical models derived from simple beam theory are elegant and convenient to apply, it is shown that these models are generally insufficient for twisted beam dynamics in the torsional and axial cases. The paper is organized as follows. In Section 2, the RCSA equations for torsional and axial response predictions are presented. A comparison between experimental and predicted results for torsional and axial receptances of a simple structure with free–free boundary conditions is provided in Section 3 to demonstrate the concepts. The RCSA equations for tool point torsional and axial predictions are developed in Section 4. This includes the "inverse RCSA" approach used to identify the spindle-machine dynamics using a standard artifact inserted in the spindle. Experimental results for a rolling element-bearing spindle with two tool-holder combinations are shown in Section 5. A discussion of the results is given in Section 6 and conclusions are included in Section 7.

* Tel.: +1 352 392 8909; fax: +1 352 392 1071.
E-mail address: tschmitz@ufl.edu.

0141-6359/$ – see front matter © 2009 Elsevier Inc. All rights reserved.
doi:10.1016/j.precisioneng.2009.08.005

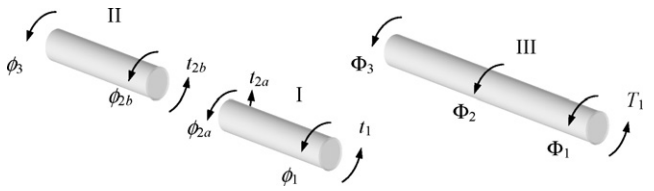

Fig. 1. Rigid coupling of components I and II to form assembly III. An external torque T_1 is applied to determine the assembly receptances S_{11} and S_{31}.

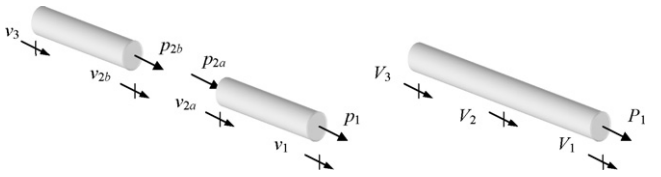

Fig. 2. Rigid coupling of components I and II to form assembly III. An external axial force P_1 is applied at V_1 to determine the assembly receptances A_{11} and A_{31}.

2. Torsional and axial receptance coupling equations

In this section the procedures are described for coupling torsional and axial receptances of components to predict assembly responses. As a convenience to the reader, closed-form receptance expressions for uniform beams with free–free (unconstrained) boundary conditions are provided in Appendix A [14]. These expressions give the complex, frequency dependent behavior of uniform beams with harmonic external torque (torsional vibration) and axial loads (axial vibration) applied. However, they are limited in application (i.e., uniform cross-section slender beams).

2.1. Torsional receptance coupling equations

As depicted in Fig. 1, given the individual receptances of two components, I and II, they may be coupled to produce the assembly, III. If the direct torsional receptance at assembly coordinate 1 is desired, an external harmonic torque with magnitude T_1 is applied at assembly coordinate 1, labeled Φ_1 (note the use of lower case variables for components and upper case variables for assemblies). In Fig. 1, it is assumed that coordinates ϕ_1 (on component I) and Φ_1 (on assembly III) are spatially collocated before and after a rigid coupling. The coupling coordinates are ϕ_{2a} and ϕ_{2b}. The free–free component direct and cross receptances are: $s_{11} = (\phi_1/t_1)$, $s_{21} = (\phi_2/t_1)$, $s_{12} = (\phi_1/t_2)$, and $s_{2a2a} = (\phi_{2a}/t_{2a})$ for I; and $s_{2b2b} = (\phi_{2b}/t_{2b})$, $s_{32b} = (\phi_3/t_{2b})$, $s_{2b3} = (\phi_{2b}/t_3)$, and $s_{33} = (\phi_3/t_3)$ for II. They may be calculated using Eqs. (A7)–(A10) (Appendix A.1) or by other available numerical or analytical techniques. The compatibility condition for the rigid coupling is $\phi_{2b} - \phi_{2a} = 0$, which enables the equality $\phi_{2a} = \phi_{2b} = \Phi_2$ to be written (Φ_2 is assumed to be collocated with ϕ_{2a} before and after the rigid coupling). Also, $\phi_1 = \Phi_1$ and $\phi_3 = \Phi_3$. The equilibrium conditions are $t_{2a} + t_{2b} = 0$ and $t_1 = T_1$.

To determine $s_{11} = (\Phi_1/T_1)$, the component torsional rotations are first written. For I, there are two torques acting on the body, so the torsional rotations are:

$$\phi_1 = s_{11}t_1 + s_{12a}t_{2a} \text{ and } \phi_{2a} = s_{2a1}t_1 + s_{2a2a}t_{2a} \tag{1}$$

For II, the torsional rotations are $\phi_{2b} = s_{2b2b}t_{2b}$ and $\phi_3 = s_{32b}t_{2b}$. Next, substitution into the compatibility condition gives:

$$s_{2b2b}t_{2b} - s_{2a1}t_1 - s_{2a2a}t_{2a} = 0. \tag{2}$$

Then, application of the equilibrium conditions enable t_1 to be replaced by T_1 and t_{2a} ($t_{2a} = t_{2b}$) to be eliminated from Eq. (2). See Eq. (3).

$$s_{2b2b}t_{2b} - s_{2a1}T_1 + s_{2a2a}t_{2b} = 0 \tag{3}$$

Grouping terms in Eq. (3) enables t_{2b} to be written as $t_{2b} = (s_{2a2a} + s_{2b2b})^{-1}s_{2a1}T_1$. Correspondingly, $t_{2a} = -(s_{2a2a} + s_{2b2b})^{-1}s_{2a1}T_1$. Finally, substitution of this torque value into the S_{11} expression gives the desired result; see Eq. (4). Note that the assembly response is written as a function of the component direct (s_{11}, s_{2a2a}, and s_{2b2b}) and cross (s_{12a} and s_{2a1}) receptances.

$$\begin{aligned} S_{11} &= \frac{\Phi_1}{T_1} = \frac{\phi_1}{T_1} = \frac{s_{11}t_1 + s_{12a}t_{2a}}{T_1} = \frac{s_{11}t_1 - s_{12a}(s_{2a2a} + s_{2b2b})^{-1}s_{2a1}T_1}{T_1} \\ S_{11} &= \frac{s_{11}T_1 - s_{12a}(s_{2a2a} + s_{2b2b})^{-1}s_{2a1}T_1}{T_1} = s_{11} - s_{12a}(s_{2a2a} + s_{2b2b})^{-1}s_{2a1} \end{aligned} \tag{4}$$

The expression for t_{2b} is used to determine the cross receptance, S_{31}. See Eq. (5).

$$\begin{aligned} S_{31} &= \frac{\Phi_3}{T_1} = \frac{\phi_3}{T_1} = \frac{s_{32b}t_{2b}}{T_1} = \frac{s_{32b}(s_{2a2a} + s_{2b2b})^{-1}s_{2a1}T_1}{T_1} \\ S_{31} &= s_{32b}(s_{2a2a} + s_{2b2b})^{-1}s_{2a1} \end{aligned} \tag{5}$$

The direct and cross receptances, S_{33} and S_{13}, respectively, may be determined by applying a torque at Φ_3. The approach is analogous and the results are included in Eqs. (6) and (7).

$$S_{33} = \frac{\Phi_3}{T_3} = s_{33} - s_{32b}(s_{2a2a} + s_{2b2b})^{-1}s_{2b3} \tag{6}$$

$$S_{13} = \frac{\Phi_1}{T_3} = s_{12a}(s_{2a2a} + s_{2b2b})^{-1}s_{2b3} \tag{7}$$

2.2. Axial receptance coupling equations

Fig. 2 depicts a rigid coupling example similar to the one shown in Fig. 1. The two free–free components I and II are coupled to produce the assembly III. To determine the direct axial receptance at the right end of the assembly, an external harmonic axial force with magnitude P_1 is applied at assembly coordinate 1, labeled V_1. Using the same assumptions and following the same steps as in Section 2.1 enables the assembly axial receptances to be written as a function of the component axial receptances. See Eqs. (8)–(11).

$$A_{11} = \frac{V_1}{P_1} = a_{11} - a_{12a}(a_{2a2a} + a_{2b2b})^{-1}a_{2a1} \tag{8}$$

$$A_{31} = \frac{V_3}{P_1} = a_{32b}(a_{2a2a} + a_{2b2b})^{-1}a_{2a1} \tag{9}$$

$$A_{33} = \frac{V_3}{P_3} = a_{33} - a_{32b}(a_{2a2a} + a_{2b2b})^{-1}a_{2b3} \tag{10}$$

$$A_{13} = \frac{V_1}{P_3} = a_{12a}(a_{2a2a} + a_{2b2b})^{-1}a_{2b3} \tag{11}$$

3. Free–free stepped beam analysis and experiments

In this section, predictions and measurements for a free–free stepped geometry beam are included. While this is a simple example, it provides a demonstration of the coupling equations and identifies the measurement challenges associated with torsional dynamics testing. The free–free boundary conditions were approximated by resting the beam on a soft foam support.

The geometry for the 1056 mm long 6061-T651 aluminum beam is shown in Fig. 3. The diameter of the end sections of the beam was 44.5 mm, while the central third of the beam length was turned to a smaller diameter of 31.4 mm. This "assembly" was then treated as three rigidly coupled components. The beam material properties were assumed to be: $E = 70$ GPa (elastic modulus), $\nu = 0.33$ (Poisson's ratio), $G = (E/2(1+\nu)) = 26.3$ GPa (shear modulus), $\rho = 2700$ kg/m^3 (density), $\eta_G = 0.0004$, and $\eta_E = 0.00015$ (solid damping factors). The

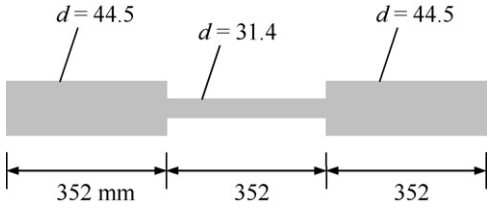

Fig. 3. Stepped diameter beam geometry.

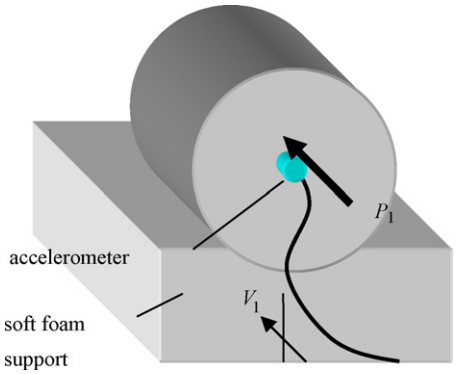

Fig. 4. The axial force P_1 was applied using the impact hammer and the V_1 axial response was measured using a low-mass accelerometer. Note that only the beam end is shown.

free–free receptances for the three beam sections were modeled and these sections were rigidly coupled to predict the assembly dynamics. Impact testing was applied to enable experimental comparison with the predicted beam receptances. In this approach, an instrumented hammer (PCB 086C04 with a sensitivity of 926 N/V for this study) is used to excite the structure and an appropriate linear transducer is used to measure the resulting response (a low-mass accelerometer, PCB 352A21 with a sensitivity of 1027 m/s^2/V for this study). A measurement bandwidth of 5000 Hz was applied, although the impact input energy above 3000 Hz was low (nylon hammer tip).

While the axial measurement was straightforward to complete (see Fig. 4), determining the torsional receptances required a special setup and a pair of complementary measurements. As shown in Fig. 5, two aluminum measurement tabs were fixed in a symmetric pattern to the beam end using cyanoacrylate. In a first measurement, the hammer impact and acceleration measurement were completed on the same tab (Fig. 5a). Because the impact was applied at a distance of 28 mm from the beam center, a torque was introduced. This excited the torsional vibration modes. However, the lateral force also effectively excited the bending modes and "corrupted" the torsional receptance. To cancel the bending

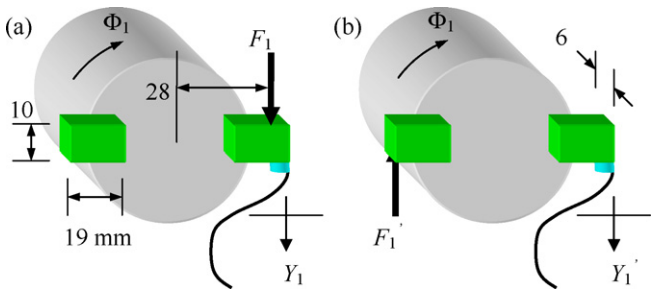

Fig. 5. (a) First torsional measurement—the lateral force F_1 was applied and the Y_1 lateral response was measured. (b) Second measurement—the lateral force F_1' was applied in the opposite direction and the Y_1' lateral response was measured.

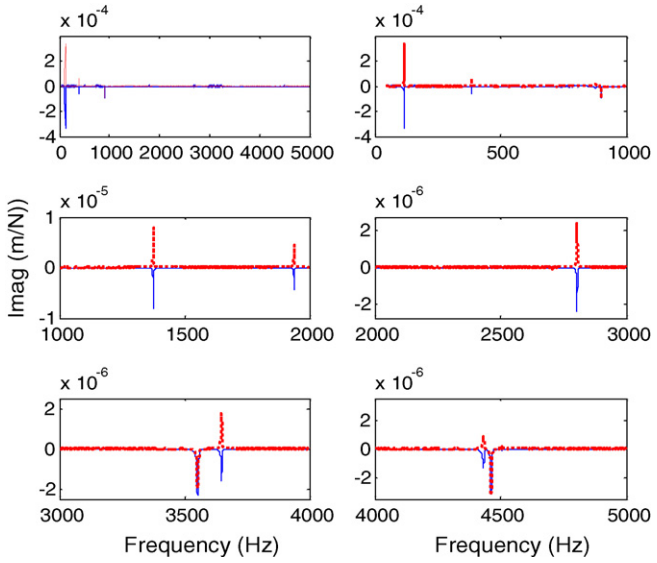

Fig. 6. Imaginary parts of first and second torsion measurements. The solid line corresponds to Fig. 5a and the dotted line to Fig. 5b. The average rejects the bending modes and isolates the torsional modes.

modes, a second measurement was completed. The accelerometer location was not changed, but the force was applied on the opposite tab at the same radius, but in the opposite direction (Fig. 5b). This caused the sign of the bending modes to reverse, but the torque direction was unchanged so the torsional response was nominally the same [18]. To reject the bending modes and isolate the torsional modes, the two measurement results were averaged on a frequency-by-frequency basis. In order to convert from the averaged acceleration-to-force (inertance or acceleration) data to rotation-to-torque data, two steps were required. First, the inertance was converted to receptance (displacement-to-force) by dividing by $-\omega^2$. Second, the torsional response was obtained from this result using Eq. (12), where r is the radius for the force application and response measurement (28 mm in Fig. 5).

$$\frac{\Phi}{T}(\omega) = \frac{Y/r}{F \cdot r} = \frac{Y}{F}(\omega) \cdot \frac{1}{r^2} \tag{12}$$

3.1. Torsional receptance coupling results

The two free–free torsional measurements described in Fig. 5 are shown in Fig. 6 for the stepped diameter aluminum beam, where the linear axis scale and frequency range have been selected for viewing convenience in the six panels. The first measurement (Fig. 5a) is identified by the solid line in all panels, while the second measurement (Fig. 5b) is identified by the dotted line. Due to the sign reversals, it is clear that the modes at 115, 386, 880, 1375, 1939, 2804, 3648, and 4463 Hz are bending modes, while the torsional modes (without sign reversals) occur at 901, 3552, and 4462 Hz.

To enable assembly predictions, the three free–free sections were described using the closed-form receptances provided in Appendix A (Eqs. (A7)–(A10) in Appendix A.1) and rigidly coupled using Eqs. (4)–(7). First, the left and middle components from Fig. 3 were coupled as shown in Fig. 7a. Second, this subassembly was coupled to the right component from Fig. 3 to give the full assembly receptances as shown in Fig. 7b. Note that a simple renumbering of the coordinates enabled the same equations to be applied two times sequentially.

A comparison between measurement and prediction is given in Fig. 8 (linear scale). The averaging approach to isolate the torsional receptances was applied for the experimental results. The

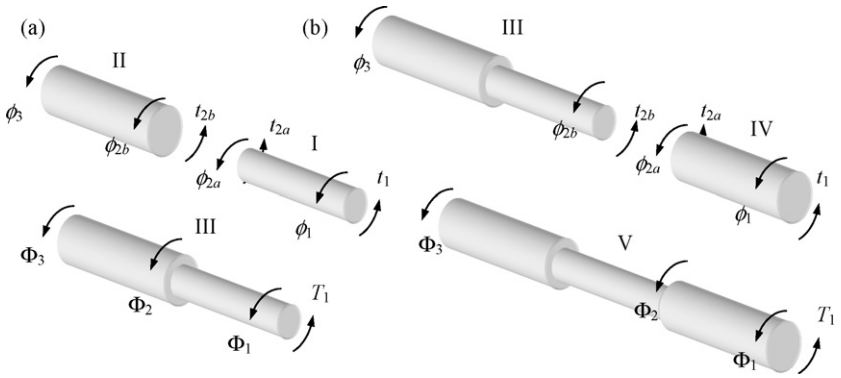

Fig. 7. (a) Rigid coupling of components I and II to form subassembly III; (b) rigid coupling of subassembly III to component IV to give assembly V.

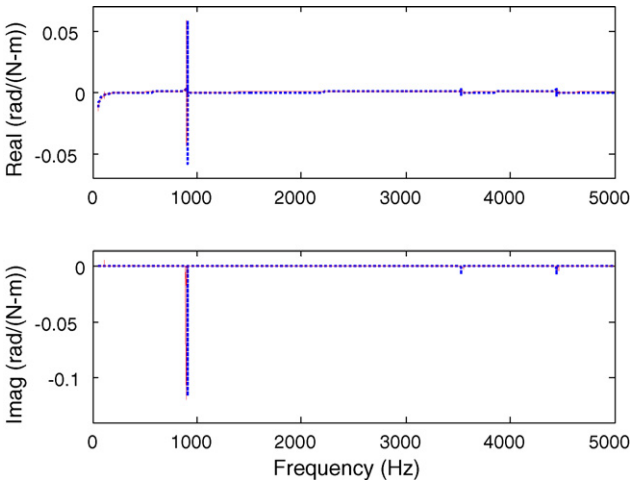

Fig. 8. Comparison between predicted (dotted) and measured (solid) torsional receptances for stepped diameter aluminum beam. The linear scale emphasizes the successful rejection of the bending modes using the averaging technique.

measured and predicted natural frequencies from Fig. 8 are 901, 3552, and 4462 Hz and 908, 3531, and 4440 Hz, respectively. This corresponding percent error between measurement and prediction is 0.8, −0.6, and −0.5%. Because the damping is very low for the free–free beam, a semi-logarithmic plot of the data in Fig. 8 is included in Fig. 9. Good agreement is again observed, although there is small residual content at the bending frequencies and the anti-resonant frequencies (near zero response) are offset. It is proposed that this offset is the result of the averaging step.

3.2. Axial receptance coupling results

Similar to the torsional receptance prediction, the three free–free stepped diameter beam sections were described using the closed-form receptances provided in Appendix A (Eqs. (A12)–(A15) in Appendix A.2) and rigidly coupled in two sequential steps using Eqs. (8)–(11) to determine the assembly's axial receptance. A comparison between measurement and prediction is provided in Fig. 10. The percent error between the measured and predicted natural frequencies, 1912 and 1937 Hz, respectively, is 1.3%. Small contributions from the bending modes are also seen in Fig. 10; it is believed that this content is observed because the force application was not exactly at the beam center, nor exactly along the beam axis.

4. Tool point receptance prediction equations

For tool-holder-spindle-machine assemblies, the RCSA approach is to couple the measured spindle-machine receptances with the modeled tool-holder receptances [10,19]. A significant step in this method is experimental identification of the spindle-machine receptances. As shown in Fig. 11, the required receptances are obtained by "inverse RCSA" where a standard artifact with the required spindle interface (e.g., CAT-40 or HSK-63A) and simple geometry is inserted in the spindle and measurements performed at the free end of this assembly. The standard

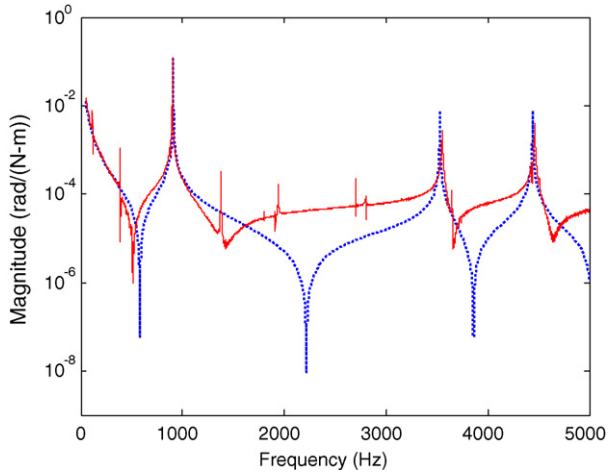

Fig. 9. Semi-logarithmic scale comparison between predicted (dotted) and measured (solid) torsional receptances for stepped diameter aluminum beam.

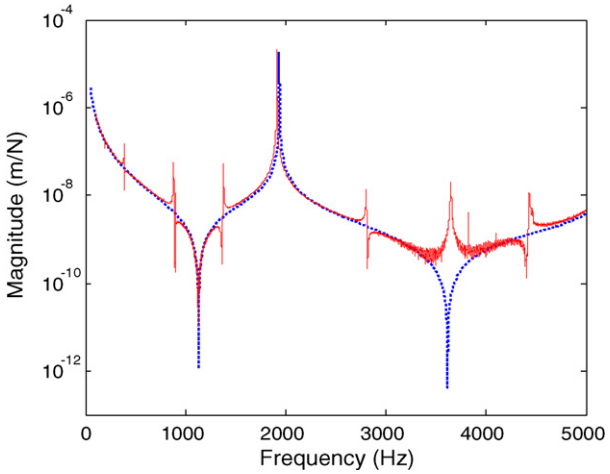

Fig. 10. Semi-logarithmic scale comparison between predicted (dotted) and measured (solid) axial receptances for stepped diameter aluminum beam.

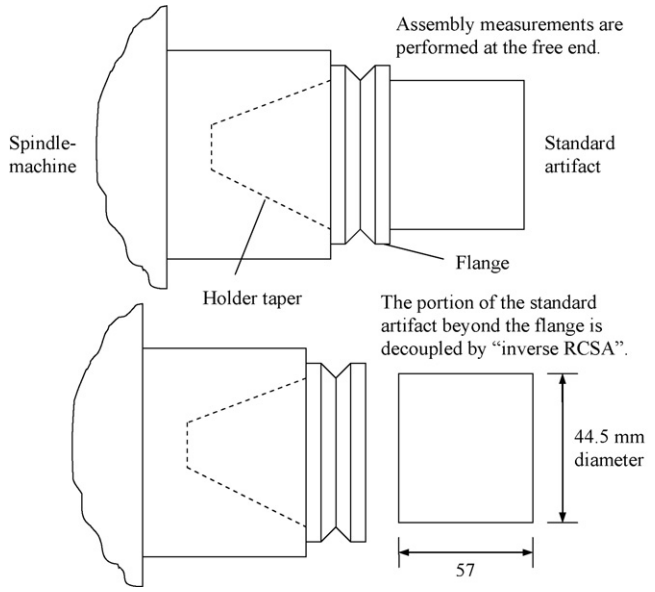

Fig. 11. A standard artifact is inserted in the spindle to identify the spindle-machine receptances using the "inverse RCSA" procedure.

artifact-spindle-machine assembly response is then decoupled to isolate the spindle-machine receptances by "removing" the portion of the standard artifact beyond the flange. Because the flange and taper are nominally identical for every holder that is inserted in a particular spindle, the holder and tool geometries (and material properties) beyond the flange for arbitrary tool-holder combinations can then be used to model the required free–free receptances. These free–free receptances are finally coupled to the experimentally identified spindle-machine response (which includes the taper connection dynamics) to identify the desired tool point assembly receptances.

4.1. Spindle-machine torsional receptances

Based on Fig. 1, the portion of the standard artifact beyond the flange (Fig. 11) may be considered to be component I and the spindle-machine (including the holder-spindle connection) to be component II. When rigidly coupled, these components form III, the artifact-spindle-machine assembly. The assembly torsional response at the free end, S_{11}, is then given by Eq. (4), where s_{11}, s_{2a1}, s_{2a2a}, and s_{12a} are the free–free receptances of the portion of the standard artifact beyond the flange and s_{2b2b} is the torsional receptance of the spindle-machine at the flange. The latter receptance is the desired spindle-machine response and may be obtained by rearranging Eq. (4) as shown in Eq. (13).

$$s_{2b2b} = s_{2a1}(s_{11} - S_{11})^{-1}s_{12a} - s_{2a2a} \tag{13}$$

As with the stepped diameter beam measurements, S_{11} was determined for the standard artifact-spindle-machine assembly using the averaging approach depicted in Fig. 5. The same aluminum measurement tabs were fixed to the free end of the standard artifact. The force excitation/measurement radius was again 28 mm. The spindle-holder interface was CAT-40 for the high-speed, rolling element-bearing spindle used in this study.

In order to determine s_{2b2b}, the torsional receptances for the spindle-machine, using Eq. (15), the free–free receptances, s_{11}, s_{2a1}, s_{2a2a}, and s_{12a}, for the portion of the steel standard artifact beyond the flange were modeled using Eqs. (A7)–(A10) (Appendix A.1), with $d = 44.5$ mm, $l = 57$ mm, $E = 200$ GPa, $\nu = 0.29$, $G = (E/2(1+\nu)) = 77.5$ GPa, $\rho = 7800$ kg/m^3, and $\eta_G = \eta_E = 0.001$. The S_{11} (measured) and s_{11}, s_{2a1}, s_{2a2a}, and s_{12a} (modeled) receptances

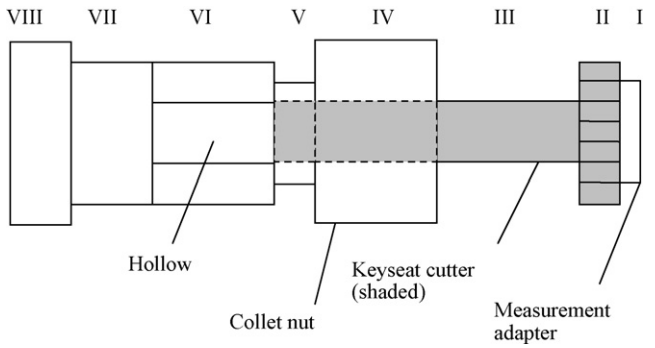

Fig. 12. Tool-holder model.

were then used to calculate the spindle-machine torsional receptance.

4.2. Spindle-machine axial receptances

The "inverse RCSA" approach was again applied to identify the spindle-machine axial receptance, a_{2b2b}; see Eq. (14). The standard artifact-spindle-machine assembly axial response, A_{11}, was measured using the approach shown in Fig. 4a and the free–free receptances for the portion of the standard artifact beyond the flange were calculated using Eqs. (A12)–(A15) (Appendix A.2).

$$a_{2b2b} = a_{2a1}(a_{11} - A_{11})^{-1}a_{12a} - a_{2a2a} \tag{14}$$

4.3. Spindle-machine bending receptances

As with the torsional and axial cases, the spindle-machine bending receptances may be determined using a model of the portion of the standard artifact beyond the flange to identify the required free–free bending receptances and measurements of the standard artifact-spindle-machine assembly measurements. The approach is detailed in [10] and is not included here for brevity.

5. Tool-holder-spindle-machine experimental results

In this section the spindle-machine receptances described in Section 4 are coupled to models of two tool-holder examples, a keyseat cutter and a standard twist drill (with three different insertion lengths). The assembly receptance predictions are then compared to measurements.

5.1. Keyseat cutter

A 38.7 mm outer diameter, 16-tooth high-speed steel keyseat cutter clamped in a steel collet holder was selected as a first testing example. This tool was chosen for convenience since it was straightforward to add an adapter which enabled the torsional excitation/measurement for experimental validation of receptance predictions. The root diameter for the keyset cutter straight teeth was 32.5 mm. For modeling purposes, the effective diameter of the cutter was assumed to be the average of the outer and root teeth diameters, 35.6 mm. The cross-sectional geometry for the tool-holder is shown in Fig. 12. It is composed of six solid cross-section steel components (II–V and VII–VIII), one hollow steel component (VI), and one solid aluminum component (I). The latter represents the measurement adapter that was fixed to the tool free end using cyanoacrylate. This adapter enabled the two torsional measurements required for rejection of the bending modes in the torsional receptances to be completed. The adapter is shown in Fig. 13 and was modeled as a circular cross-section with the same circular area as the face of the rectangular measurement adapter. Table 1 gives

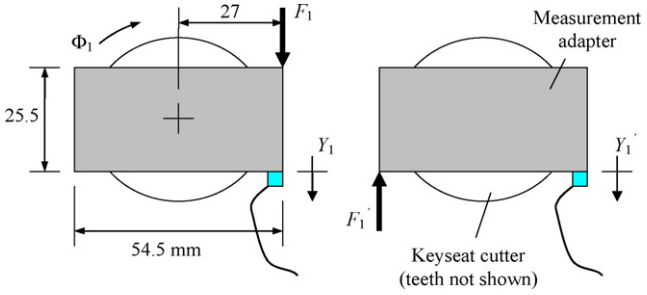

Fig. 13. Measurement adapter for keyseat tool-holder-spindle-machine torsional receptances. Two measurements were performed to cancel the bending modes.

Table 1
Keyseat cutter tool-holder components (materials are aluminum (A) and steel (S); a hollow section is indicated by (H)).

Component	Material	Inner diameter (mm)	Outer diameter (mm)	Length (mm)
I	A	–	42.1	3
II	S	–	35.6	10
III	S	–	12.7	26
IV	S	–	42.1	20
V	S	–	31.9	7
VI	S/H	12.7	40	22
VII	S	–	40	17
VIII	S	–	44.4	13

the diameters and lengths for each of the eight tool-holder components. The material properties were the same as those previously specified with $\eta_G = \eta_E = 0.001$ for both aluminum and steel.

5.1.1. Keyseat cutter assembly torsional receptances

The free–free torsional receptances for the eight components in Table 1 were calculated using Eqs. (A7)–(A10) (Appendix A.1). These were rigidly coupled as shown in Eqs. (4)–(7). The left-to-right sequential coupling approach used for the stepped diameter beam (Fig. 7) was applied to determine the free–free response of the coupled tool-holder. This subassembly was then rigidly coupled (via Eq. (4)) to the spindle-machine response, which was determined using Eq. (15) and the standard artifact torsional measurement, S_{11} (Section 4.1). A comparison between the measured and predicted responses for the tool-holder-spindle-machine assembly is provided in Fig. 14. The percent error between the measured (3120 Hz) and predicted (3130 Hz) natural frequency is 0.3%.

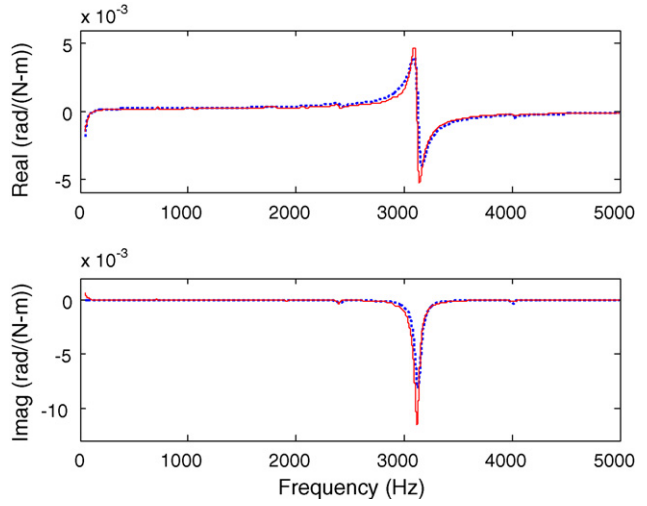

Fig. 14. Linear scale comparison between predicted (dotted) and measured (solid) torsional receptances for keyset cutter tool-holder-spindle-machine assembly.

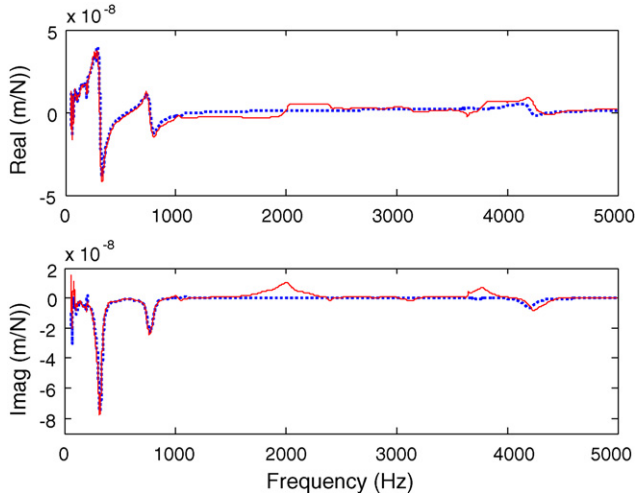

Fig. 15. Linear scale comparison between predicted (dotted) and measured (solid) axial receptances for keyseat cutter tool-holder-spindle-machine assembly.

5.1.2. Keyseat cutter assembly axial receptances

The procedure was similar to that described in Section 5.1.1. The free–free axial receptances for components II–VIII in Table 1 were calculated using Eqs. (A12)–(A15) (Appendix A.2); the measurement adapter (component I) was not required for the axial measurements. The seven components were rigidly coupled as shown in Eqs. (8)–(11) using the left-to-right sequential coupling approach to determine the free–free response of the coupled tool-holder. This subassembly was then rigidly coupled to the spindle-machine axial response (Section 4.2). A comparison between the measured and predicted responses is provided in Fig. 15. The percent error between the two dominant measured, 312 and 763 Hz, and predicted, 315 and 770 Hz, natural frequencies is, 1.0 and 0.9%. This result does not necessarily validate the tool-holder axial receptance model, which offers limited accuracy for shorter beams [14], as much as it demonstrates the importance of considering the spindle dynamics. Specifically, if the tool-holder model is coupled rigidly to ground (i.e., the spindle-machine is considered to be infinitely stiff in the axial direction), the first axial mode is seen at 12,542 Hz. The two modes observed in Fig. 15 are due to the spindle dynamics.

5.2. Twist drill

The keyseat cutter results provided in Section 5.1 demonstrate the effectiveness of the extended RCSA approach to the accurate prediction of torsional and axial receptances (bending receptance predictions have been reported previously, see, e.g. [10]). This includes the "inverse RCSA" step required for experimental identification of the spindle-machine receptances. In this section, it is shown that tool modeling is an equally important aspect of the RCSA procedure. In particular, it is seen that the simple analytical models for uniform beams included in Appendix A are not able to accurately predict the torsional-axial behavior of twisted beams.

The same spindle-machine and collet holder from the keyseat cutter experiments were used for this testing. Additionally, the spindle-machine receptances (obtained via the standard artifact) employed for the predictions in Section 5.1 were again applied. However, the keyseat cutter was replaced by a twist drill with a diameter of 12.7 mm, length of 98 mm, and shank length of 39 mm. Three different insertion lengths were applied: 39, 30, and 20 mm. In order to enable torsional and axial testing for the tool-holder-spindle-machine assembly, an aluminum measurement adapter

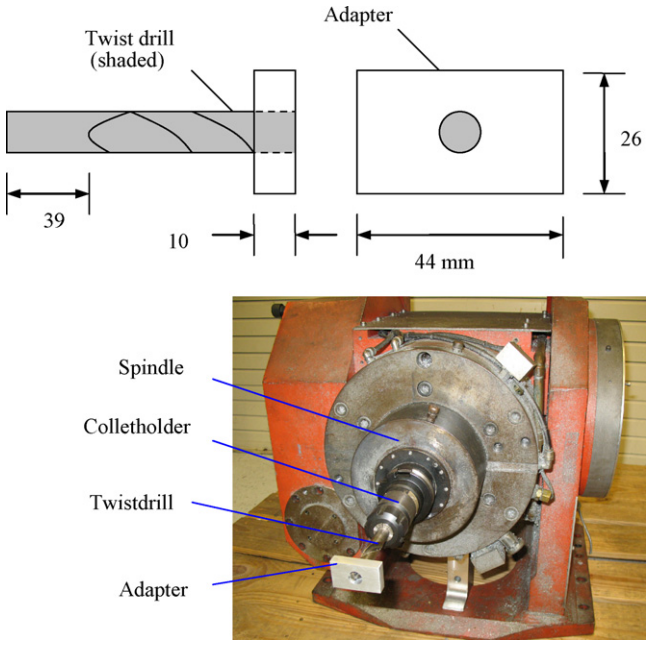

Fig. 16. Twist drill and aluminum measurement adapter geometries. The inset shows a photograph of the adapter-drill-holder clamped in the test spindle.

was again attached to the tool and included in the RCSA tool-holder model. Fig. 16 shows the adapter; the center hole was made using the test drill and then the adapter was cemented to the drill using cyanoacrylate. For modeling convenience, the rectangular adapter was represented by a cylinder with an equivalent cross-sectional area. For the 26 mm × 44 mm dimensions shown in Fig. 16, the equivalent diameter was 37.2 mm. Further, because the simple models in Appendix A require a uniform cross-section, the diameter for the fluted portion of the twist drill was approximated using a mass-based approach. Specifically, the drill mass was measured to be 72.5 g. Then, an equivalent diameter was calculated for the fluted portion which would give a two section beam (shank and fluted portion) with the measured mass. This equivalent diameter for the fluted portion was 9.6 mm.

The cross-sectional geometries for the tool-holder models are shown in Fig. 17; one each for the three insertion lengths. Table 2 gives the diameters and lengths for each of the tool-holder components in all three cases. The material properties for predictions were the same as those previously specified.

5.2.1. Twist drill assembly bending receptances

Before proceeding to the torsional and axial cases, the measured and predicted bending receptances are provided for completeness.

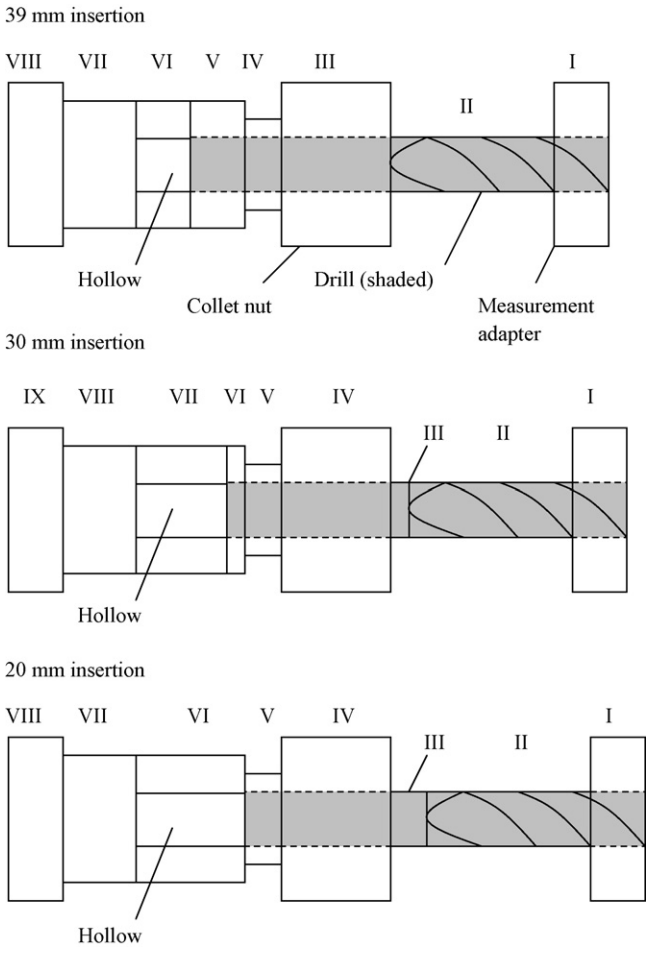

Fig. 17. Twist drill tool-holder models for three different insertion lengths. The uniform cross-sections are identified.

The free–free bending receptances for the components listed in Table 2 and depicted in Fig. 17 were calculated using a finite element solution of the Timoshenko beam equation (25 elements for each component) [10]. These components were rigidly coupled as described in [10], using the left-to-right sequential coupling approach to determine the free–free responses of the coupled tool-holder. The subassembly receptances were then rigidly coupled to the spindle-machine bending response matrix [10,20–22]. A comparison between the measured and predicted responses for the tool point displacement-to-force receptance, H_{11}, is provided in Figs. 18–20 for the three insertion lengths. Good agreement is observed in all three cases. Additionally, the interaction between

Table 2
Twist drill tool-holder components (materials are aluminum (A) and steel (S); a hollow section is indicated by (H)). The three insertions lengths for the drill are: 39 mm (1), 30 mm (2), and 20 mm (3).

Component	Material			Inner diameter (mm)			Outer diameter (mm)			Length (mm)		
	1	2	3	1	2	3	1	2	3	1	2	3
I	A/S	A/S	A/S	9.6	9.6	9.6	37.2	37.2	37.2	10	10	10
II	S	S	S	–	–	–	9.6	9.6	9.6	49	49	49
III	S	S	S	–	–	–	42.1	12.7	12.7	20	9	19
IV	S	S	S	–	–	–	31.9	42.1	42.1	7	20	20
V	S	S	S/H	–	–	12.7	40	31.9	31.9	12	7	7
VI	S/H	S	S/H	12.7	–	12.7	40	40	40	10	3	22
VII	S	S/H	S	–	12.7	–	40	40	40	17	22	17
VIII	S	S	S	–	–	–	44.4	40	44.4	13	17	13
IX		S			–			44.4			13	

Shading indicates that models 1 and 3 only have 9 components, while model 2 has 10 components.

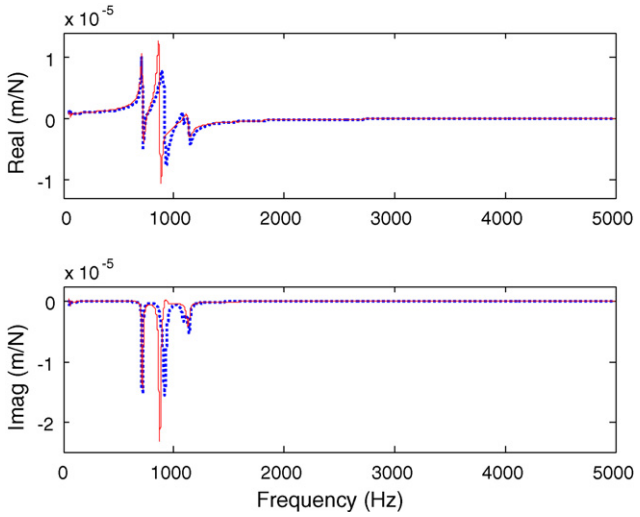

Fig. 18. Linear scale comparison between predicted (dotted) and measured (solid) bending receptances for twist drill tool-holder-spindle-machine assembly (39 mm insertion).

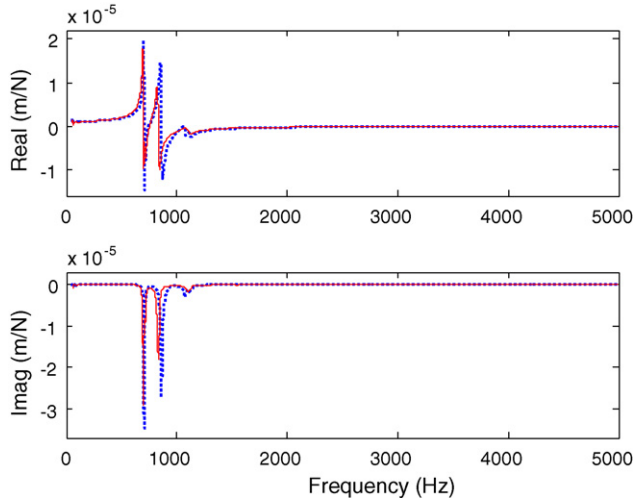

Fig. 19. Linear scale comparison between predicted (dotted) and measured (solid) bending receptances for twist drill tool-holder-spindle-machine assembly (30 mm insertion).

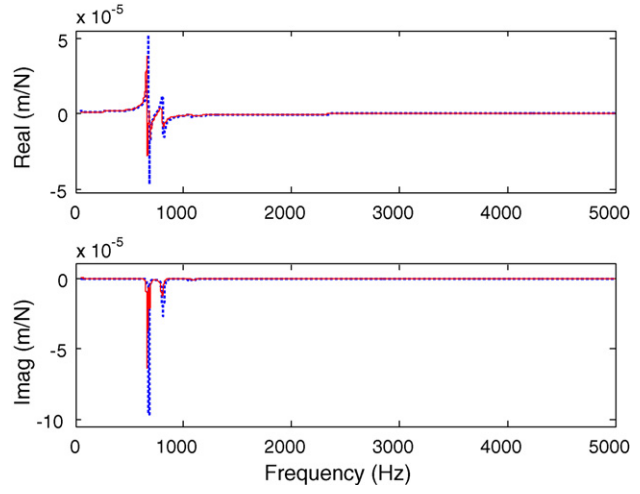

Fig. 20. Linear scale comparison between predicted (dotted) and measured (solid) bending receptances for twist drill tool-holder-spindle-machine assembly (20 mm insertion).

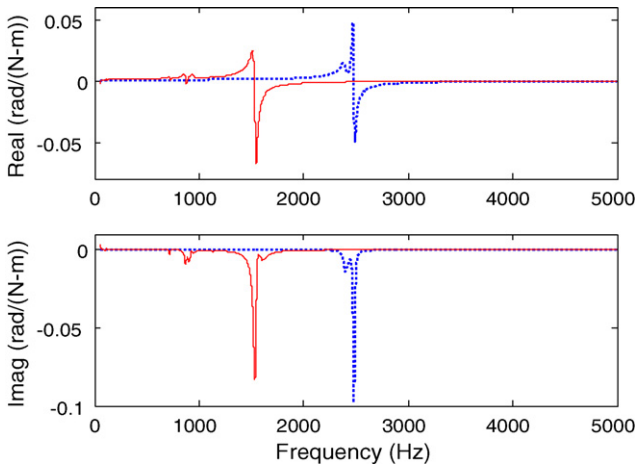

Fig. 21. Linear scale comparison between predicted (dotted) and measured (solid) torsional receptances for twist drill tool-holder-spindle-machine assembly (39 mm insertion).

the twist drill fundamental bending mode and holder-spindle-machine modes near 1000 Hz is seen [11]. This emphasizes the importance of considering the spindle-machine dynamics in assembly predictions.

5.2.2. *Twist drill assembly torsional receptances*

The free–free torsional receptances for the components in Table 2 were calculated using Eqs. (A7)–(A10) (Appendix A.1). These were rigidly coupled as shown in Eqs. (4)–(7) using the left-to-right sequential coupling approach to determine the free–free response of the coupled tool-holder. This subassembly was then rigidly coupled (Eq. (4)) to the spindle-machine response. Comparisons between the measured and predicted responses for the three twist drill tool-holder-spindle-machine assemblies are provided in Figs. 21–23. It is seen that the predicted torsional natural frequencies (dotted line) are unacceptably high relative to the measurement results (solid line) in each case. Because the twist drill fundamental torsional natural frequency is incorrect, interaction with a holder-spindle-machine mode near 2400 Hz also causes magnitude errors. This indicates that the analytical, uniform beam model included in Appendix A.1 is not adequate for twist drill torsional dynamics predictions. Residual content is also observed near 900 Hz in the measurements; this is due to imperfect canceling of

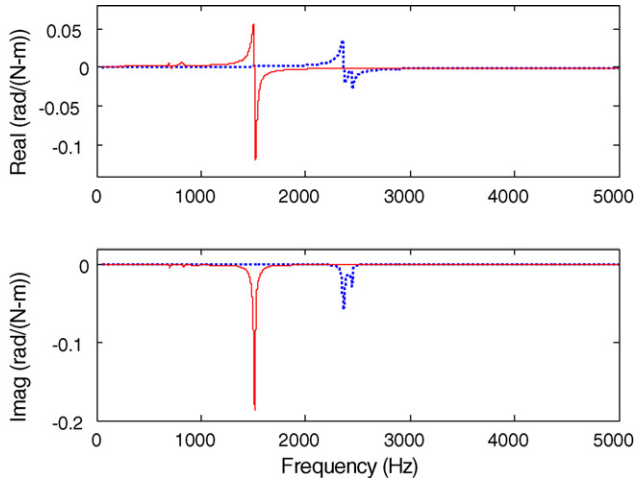

Fig. 22. Linear scale comparison between predicted (dotted) and measured (solid) torsional receptances for twist drill tool-holder-spindle-machine assembly (30 mm insertion).

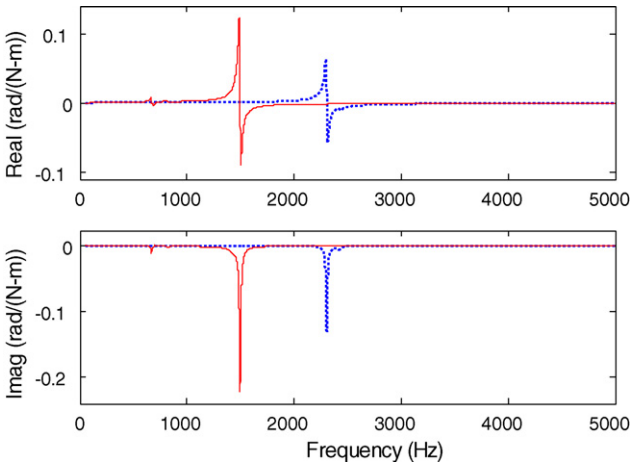

Fig. 23. Linear scale comparison between predicted (dotted) and measured (solid) torsional receptances for twist drill tool-holder-spindle-machine assembly (20 mm insertion).

the bending modes by averaging the two torsional measurements. The measurement sequence shown in Fig. 13 was applied.

5.2.3. Twist drill assembly axial receptances

For axial predictions, the free–free axial receptances for the components in Table 2 were calculated using Eqs. (A12)–(A15) (Appendix A.1). These were rigidly coupled as shown in Eqs. (8)–(11) using the left-to-right sequential coupling approach to determine the free–free response of the coupled tool-holder. This subassembly was then rigidly coupled (Eq. (8)) to the spindle-machine response. Validation measurements were next completed to compare with the assembly receptance predictions. Because it was not possible to excite and measure exactly along the tool axis and the twist drill was compliant in bending (relative to the holder and spindle), the bending modes were excited by the small couple introduced by the lateral offset between the accelerometer and hammer impact locations. To cancel the bending modes, two measurements were again performed and averaged. Fig. 24 depicts the two measurements; the accelerometer was attached to the drill point (using wax) and the force was applied above and below the

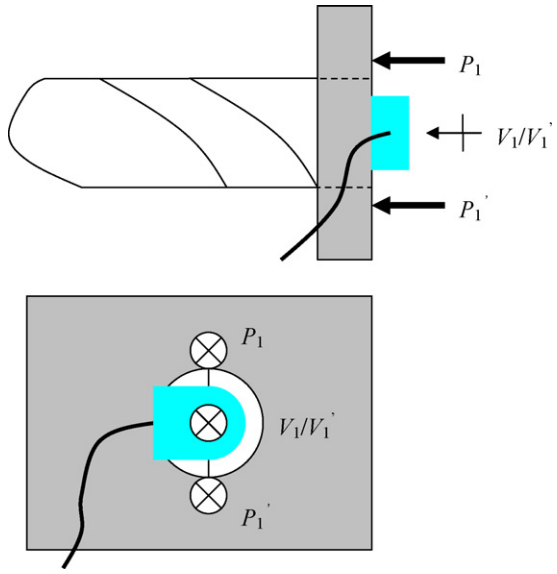

Fig. 24. Axial receptance measurements for adapter (shaded) and twist drill tool-holder-spindle-machine assembly. Two measurements were performed to cancel the bending modes.

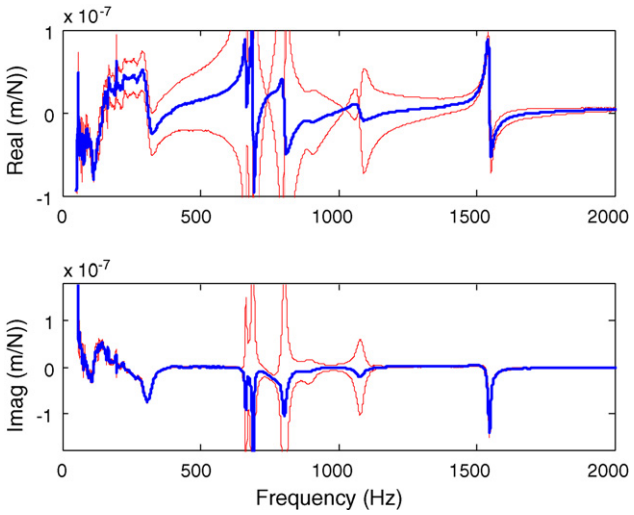

Fig. 25. Example axial measurement result for adapter and twist drill tool-holder-spindle-machine assembly. Two measurements (dotted) were averaged (solid) to isolate the axial modes. Residual bending content is observed between 700 and 1100 Hz.

accelerometer on the measurement adapter to switch the couple direction.

An example result for the 20 mm twist drill insertion length is provided in Fig. 25. In this figure, the dotted lines represent the two measurement results and the heavy solid line is the average. As expected, the bending modes between 700 and 1100 Hz switch directions. From the average, it is seen that the spindle-machine axial mode near 312 Hz seen in the keyseat cutter axial receptance results (Fig. 15) was again excited. Note that the amplitudes also match. The spindle-machine axial mode at 763 Hz is obscured by the residual bending mode content. The mode at 1547 Hz is due to the torsional-axial vibration coupling for twisted beams described in the literature [23–25]. Because the nominal measurement direction of the accelerometer is along the tool axis, it was not expected that the torsional mode would appear in the axial measurement. However, small misalignments in the axial accelerometer placement yielded some sensitivity to the subsequent torsional response. Fig. 26 shows a comparison between the averaged experimental result and prediction. As expected, the

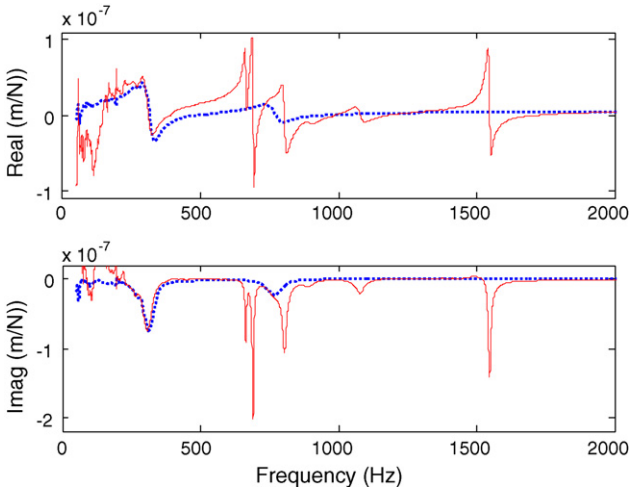

Fig. 26. Linear scale comparison between predicted (dotted) and measured (solid) axial receptances for twist drill tool-holder-spindle-machine assembly (20 mm insertion). The residual bending content between 700 and 1100 Hz is again present in the measurement data.

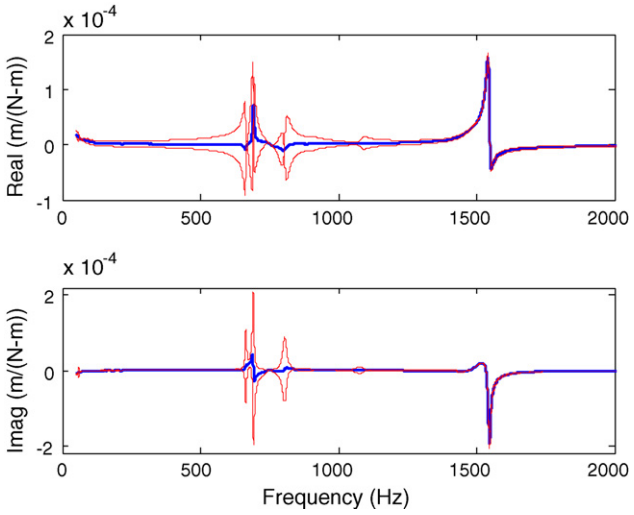

Fig. 27. Torsional excitation of axial mode. An applied torque caused axial vibration for the twist drill tool-holder-spindle-machine assembly (20 mm insertion). Two measurements (dotted) were completed in an attempt to reject the bending modes by averaging (solid).

spindle-machine axial machines appear, but no other content is present in the prediction.

To verify the torsional-axial behavior, the axial accelerometer placement was maintained, but the twist drill was excited in torsion. Again, two measurements were averaged to eliminate the bending modes (the approach shown in Fig. 13 was applied). These results are shown in Fig. 27, where the dotted lines represent the two measurements and the solid line is the average. It is seen that an axial response at 1547 Hz is obtained due to the torsional excitation, but now the spindle-machine axial modes do not appear (the torsional-axial coupling is for modes associated with the twisted beam). The conversion from axial displacement-to-force experimental data to axial displacement-to-torque data for Fig. 27 was realized using Eq. (15), where r is the radius of 21 mm for the force application on the measurement adapter.

$$\frac{V}{T}(\omega) = \frac{V}{F \cdot r} = \frac{V}{F}(\omega) \cdot \frac{1}{r} \tag{15}$$

6. Discussion

A number of conclusions can be drawn based on the comparisons of measurements and predictions in Sections 3 and 5.

1. In general, it was shown that the comprehensive RCSA approach described here could be used to select tooling (for a particular spindle-machine) that yields a desired combination of torsional, axial, and bending receptances or simply to predict the responses for existing tooling.
2. The receptance equations described here assumed a rigid connection between the tool and holder. While flexibility and damping at this interface may be included in the model, the results (excluding the torsional predictions for the twist drill, see point 3) suggest that the rigid assumption is sufficient for the macro-scale tools treated in this study. This may not be true in all situations, such as dynamic predictions for micro-scale tools or very long tool-holder combinations where the applied moment is large.
3. As with any modeling approach, there are limitations. These are highlighted for the analytical, uniform cross-section tool models applied to the twist drill predictions. It was shown that the natural frequencies for torsional modes are overpredicted and the inherent coupling between torsional and axial vibration for twisted beams is naturally not included.

The goal of this paper was to provide readers with a straightforward approach to coupling models of tools and holders with spindle-machine dynamics in order to predict torsional, axial, and bending receptances. Given this capability, the twist drill results suggest that future efforts should be focused on efficient identification of twisted beam tool free–free receptance models using numerical methods, such as finite element analysis or analytical techniques [26–28]. The motivation for torsional, axial, and bending receptance prediction is successful modeling of machining operations. Both the bending and axial receptances of tool-holder-spindle-machine assemblies can be important in ball and bull-nose end milling applications [29]; the combined torsional-axial dynamics, as well as bending responses, are required for drilling analysis [e.g., 18,30–35].

7. Conclusions

In this paper, the Receptance Coupling Substructure Analysis method is extended to prediction of torsional and axial, in addition to bending, receptances. The receptance equations for torsional and axial vibration are presented. Experimental results are compared to predictions for torsional and axial receptances of a stepped diameter free–free beam. An averaging approach, where the lateral force direction is switched but the torque direction is maintained, is used to isolate torsional modes from bending modes. Tool point torsional and axial predictions and measurements are also provided for two tool-holder-spindle-machine assemblies (bending predictions were completed for one assembly). Good agreement is generally observed, although limitations in the analytical tool models applied to a twisted beam are identified.

Acknowledgements

This work was partially supported by the National Science Foundation Grant No. DMI-0238019. Any opinions, findings, and conclusions or recommendations expressed in this material are those of the author and do not necessarily reflect the views of the National Science Foundation. The author also wishes to acknowledge C. DeMarco and A. Graziano, University of Florida, for completing initial measurements of torsional receptances for free–free beams.

Appendix A. Torsional and axial free–free receptances for uniform beams

A.1. Torsional receptances

The equation of motion for a uniform beam with a circular cross-section under torsional vibration is provided in Eq. (A1), where G is the beam material shear modulus (N/m^2), ρ is the beam material density (kg/m^3), ϕ is the rotation about the beam axis (rad), x is the position along the beam axis (m), and t is time (s) [14]. Assumptions include the following: (1) radial lines extending from the beam center to its outer diameter remain straight after an external torque is applied; and (2) shear is the only significant stress. The accuracy of this simple model is naturally limited by these assumptions.

$$G\frac{\partial^2\phi}{\partial x^2} = \rho\frac{\partial^2\phi}{\partial t^2} \tag{A1}$$

A general solution to Eq. (A1) is given by $\phi(x,t) = O(x)\,e^{i\omega t}$ for harmonic vibrations, where ω is frequency (rad/s). Calculating the second-order partial derivatives of this solution with respect to

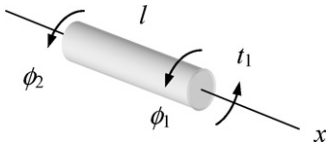

Fig. A1. Circular cross-section beam with torque applied at coordinate ϕ_1.

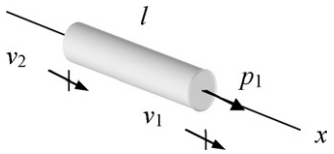

Fig. A2. Beam with axial force p_1 applied at coordinate v_1.

x and t, respectively, and substituting in Eq. (A1) yields Eq. (A2), where the exponential appears on both sides of the equality sign and is not shown.

$$G\frac{\partial^2 O}{\partial x^2} = (-\omega^2\rho)O \tag{A2}$$

A general solution to Eq. (A2) is given in Eq. (A3), where $\lambda = \omega\sqrt{\rho/G}$. In order to determine the free–free receptances at the beam ends, two boundary conditions are required. First, at a free end, $(\partial O/\partial x) = 0$. Second, for an external torque application at the beam's end, $(\partial O/\partial x) = (t_0/GJ)$, where t_0 is the harmonic torque magnitude and J is the second polar moment of area for the beam cross-section ($J = (\pi d^4/32)$ and d is the beam diameter). This boundary conditions follows from the relationship between the shear stress, τ, at radius r and the shear strain, γ, $\tau = G\gamma$, or $(t_0 r/J) = rG(d\phi/dx)$.

$$O(x) = A\cos(\lambda x) + B\sin(\lambda x) \tag{A3}$$

To develop the torsional receptances for a free–free beam, an external torque with magnitude t_1 is applied at the right end of the beam, labeled as coordinate ϕ_1 in Fig. A1, where $x = l$ and l is the beam length ($x = 0$ at the left end of the beam). The corresponding boundary conditions are provided in Eq. (A4).

$$\left.\frac{\partial O}{\partial x}\right|_{x=0} = 0 \quad \left.\frac{\partial O}{\partial x}\right|_{x=l} = \frac{t_1}{GJ} \tag{A4}$$

The coefficients A and B in Eq. (A3) are determined by calculating $(\partial O/\partial x)$ from Eq. (A3) and substituting the two boundary conditions from Eq. (A4). This gives $A = (-t_1/GJ\lambda\sin(\lambda l))$ and $B = 0$. Substitution of these coefficient values in Eq. (A3) gives Eq. (A5). Substitution of Eq. (A5) in the general solution to Eq. (A1) yields Eq. (A6).

$$O(x) = \frac{-t_1}{GJ\lambda\,\sin(\lambda l)}\cos(\lambda x) \tag{A5}$$

$$\phi_1(x,t) = O(x)\,e^{i\omega t} = \frac{-t_1}{GJ\lambda\,\sin(\lambda l)}\cos(\lambda x)\,e^{i\omega t} \tag{A6}$$

Finally, the direct torsional receptance at coordinate 1, $s_{11}(\omega)$, is written as shown in Eq. (A7) by substituting $x = l$ and converting to the frequency domain. Similarly, the cross receptance, $s_{21}(\omega)$, is determined by substituting $x = 0$ in Eq. (A6); see Eq. (A8).

$$s_{11}(\omega) = \frac{\phi_1}{t_1} = \frac{-\cos(\lambda l)}{GJ\lambda\,\sin(\lambda l)} = \frac{-\cot(\lambda l)}{GJ\lambda} \tag{A7}$$

$$s_{21}(\omega) = \frac{\phi_2}{t_1} = \frac{-\cos(\lambda\cdot 0)}{GJ\lambda\,\sin(\lambda l)} = \frac{-1}{GJ\lambda\,\sin(\lambda l)} = \frac{-csc(\lambda l)}{GJ\lambda} \tag{A8}$$

To determine the remaining two receptances, $s_{22}(\omega)$ and $s_{12}(\omega)$, for the beam, an external torque of magnitude t_2 is applied to coordinate ϕ_2 and the process is repeated. These results are given in Eqs. (A9) and (A10). In order to introduce damping in the component responses, solid (or structural) damping may be applied by replacing the shear modulus with the complex modulus $G' = G(1 + i\eta_G)$ in Eqs. (A7)–(A10), where η_G is the unitless shear damping factor. Note that λ is a function of G as well.

$$s_{22}(\omega) = \frac{\phi_2}{t_2} = \frac{-\cot(\lambda l)}{GJ\lambda} \tag{A9}$$

$$s_{12}(\omega) = \frac{\phi_1}{t_2} = \frac{-csc(\lambda l)}{GJ\lambda} \tag{A10}$$

A.2. Axial receptances

The equation of motion for a uniform beam[1] under longitudinal vibration is provided in Eq. (A11), where E is the beam material elastic modulus (N/m^2), v is the deflection along the beam axis (m), and Poisson effects are neglected. It has been shown that application of this equation yields accurate results only when the length of the bar is much larger than its cross-sectional dimensions. A ratio of at least 10:1 is suggested in [14].

$$E\frac{\partial^2 v}{\partial x^2} = \rho\frac{\partial^2 v}{\partial t^2} \tag{A11}$$

Because the equation of motion has the same form as Eq. (A1) for torsion, the free–free receptance development is similar to that provided in Appendix A.1. For brevity, only the results are provided here. For the free–free beam of length l shown in Fig. A2, application of axial force p_1 enables the receptances a_{11} and a_{21} at the beam ends to be determined. See Eqs. (A12) and (A13), where $\lambda = \omega\sqrt{\rho/E}$. As before, determining the receptances requires that two boundary conditions be applied. In this case, these are $(\partial O/\partial x) = 0$ at a free end and $(\partial O/\partial x) = (p_0/EA)$ for an external axial force application at the beam's end, where A is the beam cross-sectional area $A = (\pi d^2/4)$ for a circular beam. The latter boundary conditions follows from the relationship between the axial stress, σ, and axial strain, ε, $\sigma = E\varepsilon$, or $(p_0/A) = E(dv/dx)$. The other two receptances for the beam in Fig. A2 are determined by applying p_2 to v_2. See Eqs. (A14) and (A15). Again, in order to introduce damping in the component responses, solid damping is applied by replacing the elastic modulus with the complex modulus $E' = E(1 + i\eta_E)$ in Eqs. (A12)–(A15), where η_E is the unitless axial damping factor. Note that λ is a function of E as well.

$$a_{11}(\omega) = \frac{v_1}{p_1} = \frac{-\cot(\lambda l)}{EA\lambda} \tag{A12}$$

$$a_{21}(\omega) = \frac{v_2}{p_1} = \frac{-csc(\lambda l)}{EA\lambda} \tag{A13}$$

$$a_{22}(\omega) = \frac{v_2}{p_2} = \frac{-\cot(\lambda l)}{EA\lambda} \tag{A14}$$

$$a_{12}(\omega) = \frac{v_1}{p_2} = \frac{-csc(\lambda l)}{EA\lambda} \tag{A15}$$

References

[1] Tlusty J. Analysis of the state of research in cutting dynamics. Annals of the CIRP 1978;27(2):583–9.
[2] Smith S, Tlusty J. An overview of modeling and simulation of the milling process. Journal of Engineering for Industry 1991;113(2):169–75.
[3] Smith S, Tlusty J. Efficient simulation programs for chatter in milling. Annals of the CIRP 1993;42(1):463–6.
[4] Komanduri R. Machining and grinding: a historical review of the classical papers. Applied Mechanics Review 1993;46(3):80–132.
[5] Ehmann K, Kapoor S, DeVor R, Lazoglu I. Machining process modeling: a review. Journal of Manufacturing Science and Engineering 1997;119(4B):655–63.

[1] The beam cross-section is not required to be circular.

[6] Smith S, Tlusty J. Current trends in high-speed machining. Journal of Manufacturing Science and Engineering 1997;119(4B):664–6.
[7] Merchant ME. An interpretive look at 20th century research on modeling of machining. Machining Science and Technology 1998;2(2):157–63.
[8] Altintas Y, Weck M. Chatter stability of metal cutting and grinding. Annals of the CIRP 2004;53(2):619–42.
[9] Schmitz T, Duncan GS. Receptance coupling for dynamics prediction of assemblies with coincident neutral axes. Journal of Sound and Vibration 2006;289(4–5):1045–65.
[10] Schmitz T, Duncan GS. Three-component receptance coupling substructure analysis for tool point dynamics prediction. Journal of Manufacturing Science and Engineering 2005;127(4):781–90.
[11] Duncan GS, Tummond M, Schmitz T. An investigation of the dynamic absorber effect in high-speed machining. International Journal of Machine Tools and Manufacture 2005;45:497–507.
[12] Schmitz T, Davies M, Kennedy M. Tool point frequency response prediction for high-speed machining by RCSA. Journal of Manufacturing Science and Engineering 2001;123:700–7.
[13] Schmitz T, Donaldson RR. Predicting high-speed machining dynamics by substructure analysis. Annals of the CIRP 2000;49(1):303–8.
[14] Bishop RED, Johnson DC. The mechanics of vibration. London: Cambridge University Press; 1960.
[15] Tlusty J, Zaton W, Ismail F. Stability lobes in milling. Annals of the CIRP 1983;32(1):309–13.
[16] Altintas Y, Budak E. Analytical prediction of stability lobes in milling. Annals of the CIRP 1995;44(1):357–62.
[17] Schmitz T, Mann B. Closed form solutions for surface location error in milling. International Journal of Machine Tools and Manufacture 2006;46:1369–77.
[18] Bayly P, Metzler S, Schaut A, Young K. Theory of torsional chatter in twist drills: model, stability analysis and composition to test. Journal of Manufacturing Science and Engineering 2001;123:552–61.
[19] Schmitz T, Smith KS. Machining dynamics: frequency response to improved productivity. New York: Springer; 2009.
[20] Burns T, Schmitz T. Receptance coupling study of tool-length dependent dynamic absorber effect. In: Proceedings of American society of mechanical engineers international mechanical engineering congress and exposition, IMECE2004-60081. 2004.
[21] Burns T, Schmitz T. A study of linear joint and tool models in spindle-holder-tool receptance coupling. In: Proceedings of 2005 American society of mechanical engineers international design engineering technical conferences and computers and information in engineering conference, DETC2005-85275. 2005.
[22] Park S, Altintas Y, Movahhedy M. Receptance coupling for end mills. International Journal of Machine Tools and Manufacture 2003;43:889–96.
[23] Hodges DH. Torsion of pretwisted beam due to axial loading. ASME Journal of Applied Mechanics 1980;47:393–7.
[24] Knowles JK, Reissner E. Torsion and extension of helicoidal shells. ASME Journal of Applied Mechanics 1960;17:409–22.
[25] Finnie I, Bailey JJ. An experimental study of drill string vibration. ASME Journal of Engineering for Industry 1960;(May):129–35.
[26] Yagci B, Filiz S, Romero LL, Ozdoganlar OB. A spectral-Tchebychev technique for solving linear and nonlinear beam equations. Journal of Sound and Vibration 2009;321(1–2):375–404.
[27] Filiz S, Ozdoganlar OB, Romero LL. An analytical model for micro-endmill dynamics. Journal of Vibration and Control 2008;14(8):1125–50.
[28] Filiz S, Cheng C-H, Powell K, Schmitz T, Ozdoganlar OB. An improved tool-holder model for RCSA tool-point frequency response prediction. Precision Engineering 2009;33(1):26–36.
[29] Altintas Y. Analytical prediction of three dimensional chatter stability in milling. JSME International Journal Series C 2001;44(3):717–23.
[30] Eslimy-Isfahany SHR, Banerjee JR, Sobey AJ. Response of a bending-torsion coupled beam to deterministic and random loads. Journal of Sound and Vibration 1996;195(2):267–83.
[31] Yigit AS, Christoforou AP. Coupled torsional and bending vibrations of drill strings subject to impact with friction. Journal of Sound and Vibration 1998;215(1):167–81.
[32] Arvajeh T, Ismail F. Machining stability in high speed drilling, part 2: time domain simulation of a bending-torsional model and experimental validations. International Journal of Machine Tools and Manufacture 2006;46:1573–81.
[33] Roukema J, Altintas Y. Time domain simulation of torsional–axial vibrations in drilling. International Journal of Machine Tools and Manufacture 2006;46:2073–85.
[34] Roukema J, Altintas Y. Generalized modeling of drilling vibrations, part I: time domain model of drilling kinematics, dynamics and hole formation. International Journal of Machine Tools and Manufacture 2007;47:1455–73.
[35] Roukema J, Altintas Y. Generalized modeling of drilling vibrations, part II: chatter stability in frequency domain. International Journal of Machine Tools and Manufacture 2007;47:1474–85.